J. Prada,[1] *D. Fratta,*[2] *and J. C. Santamarina*[3]

Tomographic Detection of Low-Velocity Anomalies with Limited Data Sets (Velocity and Attenuation)

REFERENCE: Prada, J., Fratta, D., and Santamarina, J. C., **"Tomographic Detection of Low-Velocity Anomalies with Limited Data Sets (Velocity and Attenuation),"** *Geotechnical Testing Journal,* GTJODJ, Vol. 23, No. 4, December 2000, pp. 472–486.

ABSTRACT: Inherent physical difficulties associated with the effect of low-velocity anomalies on wave propagation, limited data sets, and restricted illumination angles affect the tomographic assessment of piles, caissons, slurry walls, and other similar geotechnical systems. This study evaluates various inversion methodologies for the tomographic detection of low-velocity anomalies. Travel time and amplitude data are gathered in the laboratory by simulating realistic field conditions. The inversion methodology involves data preprocessing, fuzzy logic constraining, and various forms of tomographic inversion based on either pixel or parametric representations of the medium. It is shown that the tradeoff between variance and resolution in pixel-based inversions can be overcome by adding information, such as regularized solutions, or by capturing the problem in parametric form for a presumed simple geometry. Results show that amplitude-based inversion may be more advantageous than time-based inversion in the detection of low-velocity anomalies; however, consistent coupling of transducers is required. The most robust inversion method tested in this study for the detection of low-velocity anomalies under standard field situations (i.e., limited data and restricted illumination angles) involves a combination of fuzzy logic constraining followed by parametric-based inversion.

KEYWORDS: nondestructive testing, elastic waves, ultrasound, velocity, attenuation, inverse problems, tomography, piles, caissons, columns, beams

Nomenclature

- A Amplitude, V
- B Normalized amplitude
- E Error norm, s or V
- L Length, m, travel length, m
- M Number of measurements
- N Number of measurements
- Q Matrix of touched pixels
- s Slowness, s/m
- T Transmission coefficient
- t Travel time, s
- V Wave velocity m/s
- x, y Coordinates, m
- α Attenuation coefficient, l/m
- β Geometric attenuation exponent
- η Damping coefficient
- λ Wavelength, m
- ρ Regularization coefficient

Low-velocity anomalies such as cracks, cavities, honeycombs, necking, and localized degradation can be very detrimental to the engineering performance of piles, caissons, and slurry walls. Several nondestructive techniques have been proposed and attempted to detect anomalies (Samman and O'Neil 1997; Wong 1995; Llopis and Ballard 1995; see Sansalone and Carino 1991 for a discussion of stress wave methods in NDT of concrete). Tomography is an alternative. In this case, boundary measurements are inverted to render a tomographic image of the spatial distribution of material parameters within the body; the intent is to visualize the presence of anomalies in the image.

However, there are several inherent difficulties in tomographic imaging. First, straight-ray tomography presumes that travel paths are zero-thickness straight lines. This assumption is valid when the wave frequency is infinite and velocity changes within the host medium are smaller than about 30% (Santamarina 1994). Low-velocity anomalies often present much higher contrast; in this case, nonlinear inversion procedures may be required.

Second, when the wavelength λ approaches the main dimension of the inclusion, diffraction prevails. In the diffraction regime, waves bend around low-velocity inclusions effectively masking their presence. This situation is sometimes referred to as "diffraction healing" (Potts and Santamarina 1993). Under these conditions, the straight-ray assumption adds model error to the inversion and degrades the quality of the tomographic image [Kak and Slaney 1988; Devaney 1984; Gelius (1995) presents a diffraction solution methodology for nonuniform background and uses synthetic data to validate the solution].

Third, buried structures such as piles and walls can be illuminated in limited directions, in contrast to medical tomograms which are gathered by illuminating the body in 360 deg. Restricted illumination hinders the constraining of the anomaly in the prevailing direction of wave propagation.

Fourth, scatterers near the ray path affect the arriving wave fronts. Consider a source and a receiver separated by a distance L. The ellipsoid drawn with a cord of length $L + \lambda/4$, with foci at the source and receiver locations, delimits the region sampled by the wave front (this is known as Fresnel's ellipsoids); if multiple reflectors are present, the cord length becomes $L + \lambda/2$ (Nolet 1987). Therefore, closely spaced sources and receivers tend to sample similar regions; thus, a high number of closely spaced measurements does not necessarily indicate independent information. The

[1] Geotechnical engineer, Parsons Brinckerhoff, New York, NY.
[2] Assistant professor, Civil Engineering, Louisiana State University, Baton Rouge, LA 70803.
[3] Professor, School of Civil and Environmental Engineering, Georgia Institute of Technology, Atlanta, GA 30332-0355.

size of ellipses and their superposition will decrease with shorter wavelengths, i.e., higher frequencies. Vasco et al. (1995) present a travel time tomographic solution that uses Frenel's ellipsoids. In this approach, the time of first arrival is replaced for the time at the first peak, which is easier to determine.

This paper documents a tomographic study designed to simulate realistic field measurements, i.e., small data sets and restricted illumination angles, in the search for low-velocity anomalies. Both amplitude and travel time data are considered within the first-order linear approximation of straight rays and with an effective curved ray model. Tomographic inversions are obtained using pixel-based and parametric-based representations of the medium.

Tomographic Inversion: Pixel-Based Representation

Tomographic inversion in terms of pixel values starts by subdividing the region into pixels of constant material properties (Fig. 1*a*). The distance traveled by the *i*th ray through the *k*th pixel determines the length $L_{i,k}$. Then, the summation of travel lengths $L_{i,k}$ times material parameters permits estimating travel time or amplitude.

Travel Time Tomography—The travel time t_i from a source to a receiver is computed by multiplying the length of ray *i* in pixel *k*, $L_{i,k}$ times the slowness of pixel *k*, s_k (inverse of the pixel velocity V_k), and adding for all pixels touched by the *i*th ray (see Fig. 1*a*):

$$t_i^{\langle\text{meas}\rangle} = \sum_k \frac{L_{i,k}}{V_k} = \sum_k L_{i,k} \cdot s_k \tag{1}$$

In matrix form:

$$\underbrace{\underline{t}^{\langle\text{meas}\rangle}}_{\text{known}} = \underbrace{\underline{\underline{L}}}_{\text{known}} \cdot \underbrace{\underline{s}}_{\text{unknown}} \tag{2}$$

where $\underline{t}^{\langle\text{meas}\rangle}$ is the vector of measured travel times, $\underline{\underline{L}}$ is the matrix of estimated pixel travel lengths, and $\underline{s}$ is the vector of unknown pixel slowness.

Amplitude Tomography—The wave front attenuates as it propagates through the medium. Three different effects cause this attenuation: expansion of the wave front (geometric attenuation), reflection at interfaces, and energy loss within the material (material attenuation). The following equation captures these three causes of attenuation:

$$A_i^{\langle\text{meas}\rangle} = A_o \cdot \left(\frac{L_o}{\sum_k L_{i,k}} \right)^{\beta} \cdot \left(\prod_k T_k \right) \cdot e^{-\sum_k L_{i,k} \cdot \alpha_k} \tag{3}$$

where $A_i^{\langle\text{meas}\rangle}$ is the amplitude measured at the end of ray *i*, A_o is the amplitude measured at an arbitrary distance L_o, T_k is the transmission coefficient between pixel *k* and its neighbor, the β exponent reflects the geometry of the propagating front (in terms of amplitude: $\beta = 0.5$ for cylindrical and $\beta = 1$ for spherical wave front), and α_k is the material attenuation coefficient in pixel *k*. The directivity of sources and receivers is assumed spherical in Eq 3. Furthermore, the transmission coefficient between pixels can be assumed ~100% in quasi-homogeneous media ($T_k = 1$ and $\prod T_k = 1$). Then, taking the logarithm on both sides, Eq 3 becomes:

$$-\ln \left[\frac{A_i^{\langle\text{meas}\rangle}}{A_o} \left(\frac{\sum_k L_{i,k}}{L_o} \right)^{\beta} \right] = \sum_k L_{i,k} \cdot \alpha_k \tag{4}$$

In matrix form, Eq 4 can be written as:

$$\underbrace{\underline{B}^{\langle\text{meas}\rangle}}_{\text{known}} = \underbrace{\underline{\underline{L}}}_{\text{known}} \cdot \underbrace{\underline{\alpha}}_{\text{unknown}} \tag{5}$$

where the vector $\underline{B}^{\langle\text{meas}\rangle}$ includes the natural logarithm of the normalized measured amplitudes corrected for geometric spreading (the denominator $A_o L_o^{\beta}$ is a constant; its true value remains unknown in most applications), $\underline{\underline{L}}$ is the matrix of travel lengths, and $\underline{\alpha}$ is the vector of unknown attenuation coefficients.

Matrix Inversion—The goal of tomographic inversion is to solve for the vector of unknown pixel values. From Eqs 2 and 5,

$$\underline{s}^{\langle\text{pred}\rangle} = \underline{\underline{L}}^{\langle\text{inverse}\rangle} \cdot \underline{t}^{\langle\text{meas}\rangle} \tag{6}$$

and

$$\underline{\alpha}^{\langle\text{pred}\rangle} = \underline{\underline{L}}^{\langle\text{inverse}\rangle} \cdot \underline{B}^{\langle\text{meas}\rangle} \tag{7}$$

where $\underline{s}^{\langle\text{pred}\rangle}$ and $\underline{\alpha}^{\langle\text{pred}\rangle}$ are the vectors of predicted pixel values for slowness and attenuation respectively. The matrix $\underline{\underline{L}}$ is either singular and/or nonsquare in most cases. Various forms of the least-squares solution can be applied (Table 1—details can be found in Santamarina and Fratta 1998):

- The Least Squares Solution (LSS—Solution 1 in Table 1) applies to over-determined problems.
- The Damped Least-Squares Solution (DLSS—Solution 2 in Table 1) allows solving mixed-determined problems. This is the prevailing condition in geotechnical engineering applications.
- The Regularized Least-Squares Solution (RLSS—Solution 3 in Table 1) incorporates information by means of a regularization matrix. For example, the regularization matrix permits smoothing the second derivative of the solution. Previous studies show that regularization is very effective in mixed-determined problems such as cross-hole tomography (Gheshlaghi and Santamarina 1998; Samani 1997 presents a theoretical approach for the tomographic imaging of state of stress in soils using regularization solutions).
- In many cases, an initial estimate of pixel values is available (e.g., host medium property) or can be readily generated by preprocessing the measurements (e.g., cross-hole data). This estimate is incorporated to the inversion as shown in Table 1—Solution 4.

Table 1 presents two other special solutions. The singular value decomposition provides both a methodology for inversion as well as information about the number of meaningful equations relative to the number of unknowns (SVD—Solution 5 in Table 1; Menke 1989). Finally, the "fuzzy logic constraining" algorithm (Solution 6 in Table 1) facilitates the detection of anomalies; the solution obtained is a credible initial guess to other formal inversion solutions. The method follows (Santamarina and Fratta 1998):

- Compute the average slowness or attenuation for each ray,

$$s_i = \frac{t_i^{\langle\text{meas}\rangle}}{L_i} \qquad \text{average slowness} \tag{8}$$

TABLE 1—*Selected matrix inversion methods (after Santamarina and Gheslaghi 1995).*

Solution	Criterion	Solution—Estimate
1. LSS	min($\underline{e}^T\cdot\underline{e}$)	$\underline{s}^{<est>} = (\underline{\underline{L}}^T\cdot\underline{\underline{L}})^{-1}\cdot\underline{\underline{L}}^T\cdot\underline{t}^{<meas>}$
2. DLSS	min [$\underline{e}^T\cdot\underline{e} + \eta^2\cdot\underline{s}^T\cdot\underline{s}$]	$\underline{s}^{<est>} = (\underline{\underline{L}}^T\cdot\underline{\underline{L}} + \eta^2\cdot\underline{\underline{I}})^{-1}\cdot\underline{\underline{L}}^T\cdot\underline{t}^{<meas>}$
3. RLSS	min [$\underline{e}^T\cdot\underline{e} + \rho\cdot(\underline{\underline{R}}\cdot\underline{s})^T\cdot(\underline{\underline{R}}\cdot\underline{s})$] $\underline{\underline{R}}$ regularization operator ρ regularization coefficient	$\underline{s}^{<est>} = (\underline{\underline{L}}^T\cdot\underline{\underline{L}} + \rho\cdot\underline{\underline{R}}^T\cdot\underline{\underline{R}})^{-1}\cdot\underline{\underline{L}}^T\cdot\underline{t}^{<meas>}$
4. RLSS with initial guess $\underline{s}_o$	Replace: $\underline{t}\rightarrow(\underline{t}^{<meas>} - \underline{\underline{L}}.\underline{s}_o)$	$\underline{s}^{<est>} = \underline{s}_o + (\underline{\underline{L}}^T\cdot\underline{\underline{L}} + \rho\cdot\underline{\underline{R}}^T\cdot\underline{\underline{R}})^{-1}\cdot\underline{\underline{L}}^T\cdot\underline{t}^{<meas>} - \underline{\underline{L}}\cdot\underline{s}_o)$
5. SVD	Factorization of $\underline{\underline{L}} = \underline{\underline{U}}\cdot\underline{\underline{\Lambda}}\cdot\underline{\underline{V}}^T$ Columns of $\underline{\underline{U}}$: eigenvectors of $\underline{\underline{L}}\cdot\underline{\underline{L}}^T$ Columns of $\underline{\underline{V}}$: eigenvectors of $\underline{\underline{L}}^T\cdot\underline{\underline{L}}$ $\Lambda_{i,i} = \lambda_i$ and $\Lambda_{i,h} = 0$ for $i \neq h$ λ_i sqrt eigenvalues of $\underline{\underline{L}}\cdot\underline{\underline{L}}^T$ or $\underline{\underline{L}}^T\cdot\underline{\underline{L}}$	$\underline{s}^{<est>} = \underline{\underline{V}}^{<p>}\cdot(\underline{\underline{\Lambda}}^{<p>\,-1}\cdot(\underline{\underline{U}}^{<p>})^T\cdot\underline{t}^{<meas>}$ (keeping $\lambda_1 \geq \ldots \geq \lambda_p \geq 0$)
6. Fuzzy logic constraining	Constrain the inclusion by determining where it cannot be The results can be used as initial guess $\underline{s}_o$	Avg. slowness $_i = \dfrac{t_i^{<meas>}}{\sum_k L_{i,k}}$ Assign the ith average parameter to all pixels touched by the ith ray. Arrange in a matrix $\underline{\underline{Q}}$. $s_k^{<min\text{–}ave>} = \min[\underline{\underline{Q}}^{<k\ column>}]$ $s_k^{<max\text{–}ave>} = \max[\underline{\underline{Q}}^{<k\ column>}]$

NOTE: $\underline{s}_o$ is an initial guess.
The residual error is $\underline{e} = (t^{<meas>} - \underline{\underline{L}}\cdot\underline{s}^{<pred>})$.
These solutions are general, even though they are written with travel time tomography notation.

$$\alpha_i = \frac{B_i^{\langle meas\rangle}}{L_i} \qquad \text{average attenuation coefficient} \qquad (9)$$

- Assign the average value calculated with Eqs 8 and 9 to all k-pixels "touched" by the i-ray; these are the entries in the matrix $Q_{i,k}$.
- The value selected for pixel k is either the minimum or the maximum of the values in the kth column of $\underline{\underline{Q}}$, depending on whether a high or a low contrast anomaly is sought,

$$s_k^* \text{ or } \alpha_k^* = \min[\underline{\underline{Q}}^{\langle kcolumn\rangle} \qquad \text{high value anomaly} \qquad (10)$$

$$s_k^* \text{ or } \alpha_k^* = \max[\underline{\underline{Q}}^{\langle kcolumn\rangle} \qquad \text{low value anomaly} \qquad (11)$$

Equations 10 and 11 yield the pixel values used to color the tomographic image.

Tomographic Inversion: Parametric Representation of the Medium

The medium and the anomaly can be described in terms of a small number of unknown parameters. The parameters needed to describe the problem of a circular inclusion in homogeneous host medium are the velocity of the medium V_{med} (or the attenuation α_{med}), the velocity of the inclusion V_{inc} (or attenuation α_{inc}), and the location and radius of the inclusion (x_{inc}, y_{inc}, R_{inc}). The solution starts with an initial guess of the parameters. Then, travel times (or amplitudes) are computed by forward simulation; computationally effective solutions can be developed for simple models such as the one depicted in Fig. 1*b* (algorithms can be found in the authors' website). Unknown parameters are iteratively modified until a good match between computed and measured travel times (or amplitudes) is obtained. This representation applies to anomalies that are traversed by rays (Fig. 1*b*).

If the anomaly has high contrast with the medium, rays will not travel through it but around it (Fig. 1*c*—Table 2). While there is no explicit information about the properties of the inclusion V_{inc} (or α_{inc}), the properties of the host medium may be altered near the inclusion. Therefore, the velocity around the edge of the inclusion V_{edge} may be included in the list of unknowns (or the attenuation α_{edge}—see Wielandt 1987).

The main advantage of the parametric representation of the medium is reducing the number of unknowns, from hundreds of pixel values to a handful of descriptive parameters. Intrinsically, this representation incorporates information to the problem, as the geometry and number of inclusions are presumed known. The main disadvantage of this approach is the need to invoke time-consuming forward simulation in every iteration.

Experimental Study

An experimental tomographic study was designed to assesses the viability of using a small set of low-angularity data to determine the location of a low-velocity inclusion in concrete. The specimen consists of a 0.610 m length, 0.305 m wide, and 0.305 m high block. The material is lightweight concrete (Portland cement mixed with 2 mm Styrofoam beads). Lightweight concrete facilitates the implementation of the experiment without compromising the quality of the data or the interpretation of the results. The P-wave velocity in this material is approximately $V \approx 1170$ m/s. A cylindrical cavity 0.076 m in diameter is formed in the specimen (Fig. 2). The P-wave velocity in air is $V = 340$ m/s (Note: The relative impedance between the concrete and air is ~4700.)

Sources and Receivers—The impact source strikes onto metal pads cemented on the concrete. The electrical contact at impact triggers the oscilloscope (Fig. 2). Receivers are Valpey-Fisher VP-1093 piezocrystal transducers (frequency range: DC-1.2 MHz). The contact imprint of these transducers is 2.36 mm. Because amplitude tomography is critically dependent on the consistent coupling of all receivers, receivers are mounted on

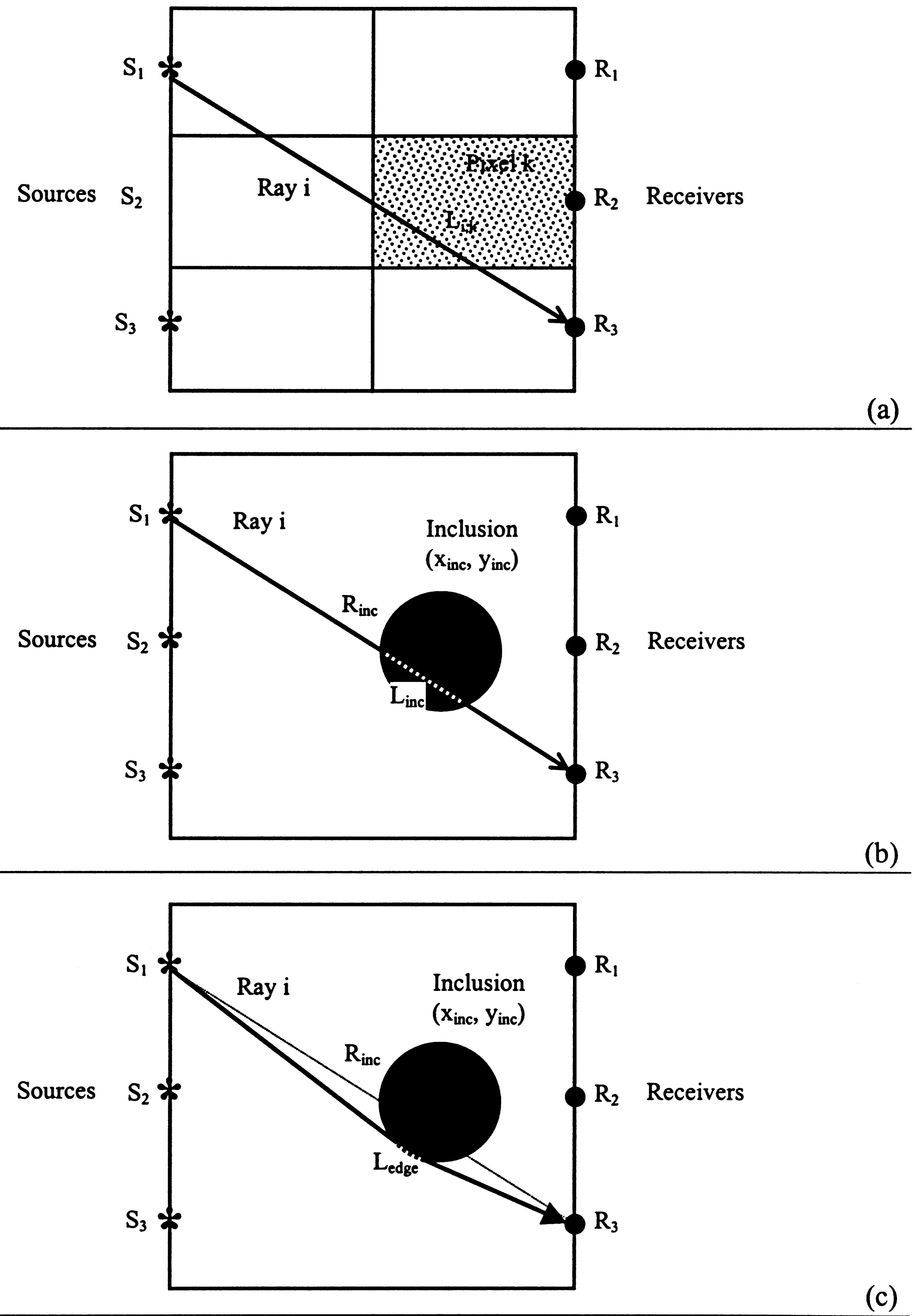

FIG. 1—*Inversion models.* (a) *Pixel representation of the medium using straight rays.* (b) *Parametric representation of the medium and straight rays.* (c) *Parametric representation of the medium and curved rays.*

spring-loaded supports and coupling is enhanced with a coupling jelly.

Consecutive sources and receivers are separated at 5.1 cm. This separation takes into consideration the expected wavelength of the propagating waves, so that two consecutive receivers can provide independent information, i.e., Fresnel's ellipses between two consecutive rays present limited overlap. Overall, the region of the anomaly is covered with six sources and six receivers producing a total of 36 signals. This is a very small data set from the point of view of tomographic detection of anomalies.

Data Acquisition—A computer-based Rapid System RS-2000 digital storage oscilloscope captures the signals with 500 kHz sampling rate. Captured signals are displayed on the screen, visually inspected, and saved into the computer hard drive (Fig. 2). No other signal processing technique is used on the raw data.

TABLE 2—*Parametric representation of medium and anomaly.*

Straight-Ray Assumption			
Travel Time Tomography		Amplitude Tomography	
Parameters:		Parameters:	
X-coordinate of inclusion:	x_{inc}	X-coordinate of inclusion:	x_{inc}
X-coordinate of inclusion:	y_{inc}	X-coordinate of inclusion:	y_{inc}
Radius of inclusion:	R_{inc}	Radius of inclusion:	R_{inc}
Slowness of inclusion:	s_{inc}	Attenuation of inclusion:	α_{inc}
Slowness of medium:	s_{med}	Attenuation of medium:	α_{med}
Model: $t^{<meas>} = \frac{(L - L_{inc})}{V_{med}} + \frac{L_{inc}}{V_{inc}}$		Model: $B^{<meas>} = (L - L_{inc})\cdot\alpha_{med} + L_{inc}\cdot\alpha_{inc}$	
where: L = ray length; $L_{inc} = f$(ray location, x_{inc}, y_{inc}, R_{inc}) is ray length across inclusion		where: L =ray length; $L_{inc} = f$(ray location, x_{inc}, y_{inc}, R_{inc}) is ray length across inclusion	
Curved-Ray Assumption			
Travel Time Tomography		Amplitude Tomography	
Parameters:		Parameters:	
X-coordinate of inclusion:	x_{inc}	X-coordinate of inclusion:	x_{inc}
X-coordinate of inclusion:	y_{inc}	X-coordinate of inclusion:	y_{inc}
Radius of inclusion:	R_{inc}	Radius of inclusion:	R_{inc}
Slowness of inclusion:	V_{edge}	Attenuation of inclusion:	α_{inc}
Slowness of medium:	V_{med}	Attenuation of medium:	α_{med}
Model: $t^{<meas>} = \frac{(L - L_{edge})}{V_{med}} + \frac{L_{edge}}{V_{edge}}$		Model: $B^{<meas>} = (L - L_{edge})\cdot\alpha_{med} + L_{edge}\cdot\alpha_{edge}$	
where: L = ray length; $L_{inc} = f$(ray location, x_{inc}, y_{inc}, R_{inc}) is ray length at edge of inclusion		where: L =ray length; $L_{inc} = f$(ray location, x_{inc}, y_{inc}, R_{inc}) is ray length at edge of inclusion	

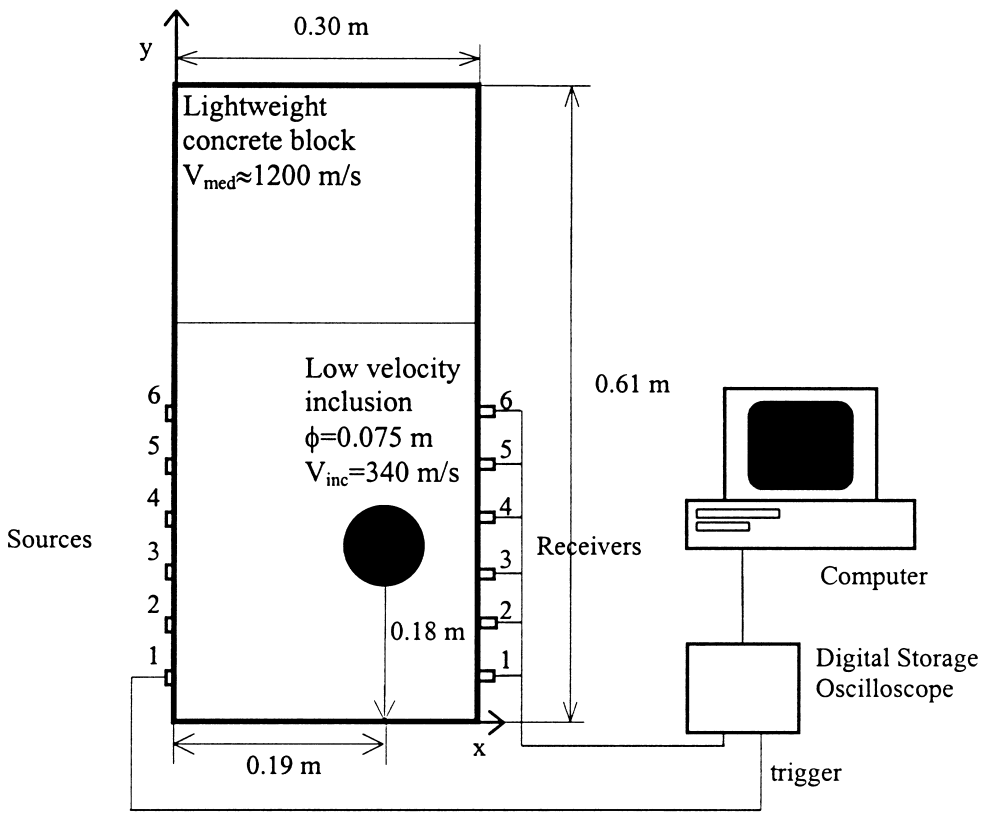

FIG. 2—*Experimental setup and peripheral electronics (trigger and receiver spacing: 51 mm).*

Data Preprocessing

Travel Times—Figure 3 shows a typical set of signals, for a given source. Figure 4*a* shows the method for picking first arrivals used in this study. While other strategies are considered, the tangent method described in the figure provides the most consistent data set. Figure 4*b* shows the average slowness "shadows" for each ray as calculated using Eq 8. Note that the back-projection of the shadows onto the space of specimen constrains the possible location of the inclusion by discarding regions where the inclusion cannot be. This observation leads to the graphical implementation of the fuzzy logic constraining procedure.

Amplitude—Two different methods are tested to assess the energy arriving at each transducer (Fig. 5*a*). The first method consists of selecting the amplitude of the first peak. The second method integrates the square of the signal from time zero to the first peak (this time restriction avoids adding the effect of boundary reflections). The first method yields a more consistent data set. Figure 5*b* presents the shadows of average attenuation along each ray computed with Eq 9, where the values L_o and A_o are taken as $L_o = 0.305$ m and $A_o = 0.150$ V. It is important to note that amplitude data are not corrected for the directivity of sources and receivers. This correction is often difficult in field measurements (see White 1983 for theoretical directivity functions and Fratta 1999 for an experimental determination).

Figures 4*b* and 5*b* show that the anomaly yields more contrasting shadows in terms of average attenuation (about 100% contrast) than in terms of average velocity (about 10% contrast). Yet, contrast alone is not sufficient for a successful inversion: the signal-to-noise ratio can be equally or more important. Figures 4*b* and 5*b* show similar signal-to-noise ratio for both data sets.

Spatial Coverage—The total length traveled by all rays in each pixel is a rough but meaningful indicator of the spatial distribution of information. Figure 6*a* presents the spatial coverage for three pixel resolutions (6×6, 5×5, and 4×4). The spatial coverage in all three cases is uneven, with information densely concentrated at the center of the image and sparse coverage at the edges (cross-hole tomographic problems are mixed-determined in most cases). Minimum and maximum values of travel length per pixel are shown for each resolution level (values are normalized with respect to pixel width). Clearly, the coverage of each pixel decreases as the number of pixels increases. It is important to note that the anomaly is located away from the region of maximum spatial coverage, making its detection more difficult (Figs. 2 and 6).

Singular Value Decomposition—Not all rays (i.e., equations) are independent; for example, neighboring rays may yield the same information about some pixels. This situation worsens as the number of pixels decreases. Singular value decomposition allows making an informed assessment of the number of independent equations in a system. Figure 6*b* shows the sorted singular values for the three cases presented in Fig. 6*a*. As the number of pixels increases, the number of nonzero singular values increases as well indicating that more information is extracted from the data. However, the number of unknowns increases at a faster rate, therefore the degree of under-determination increases.

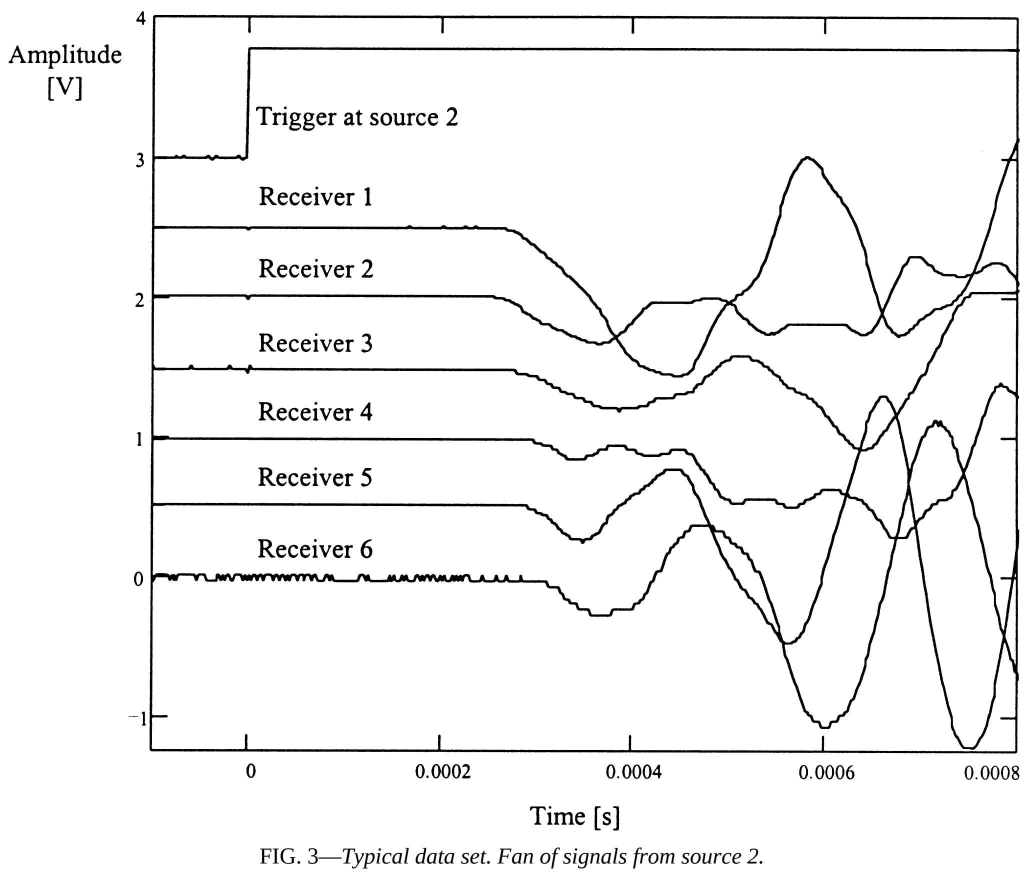

FIG. 3—*Typical data set. Fan of signals from source 2.*

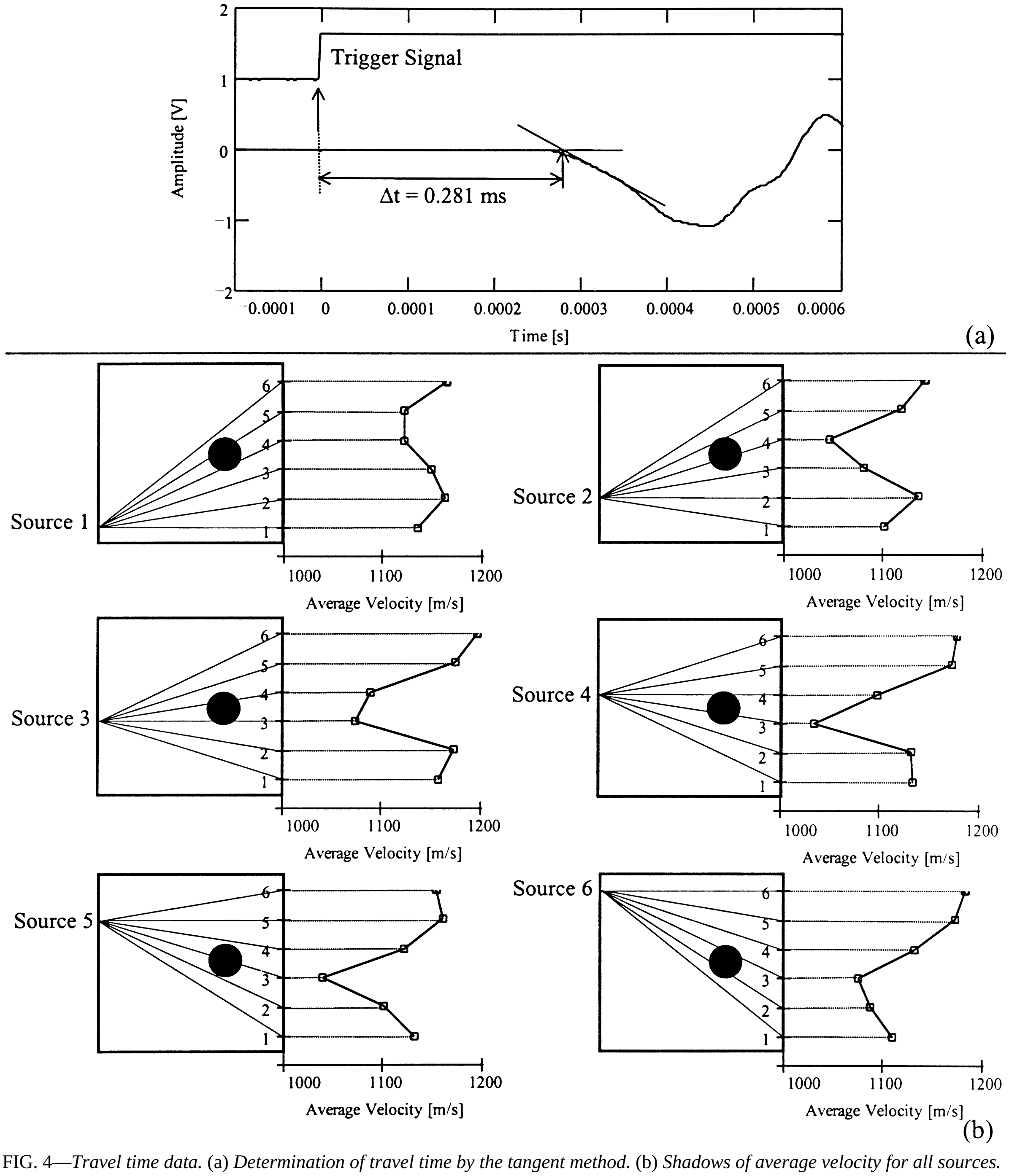

FIG. 4—*Travel time data.* (a) *Determination of travel time by the tangent method.* (b) *Shadows of average velocity for all sources.*

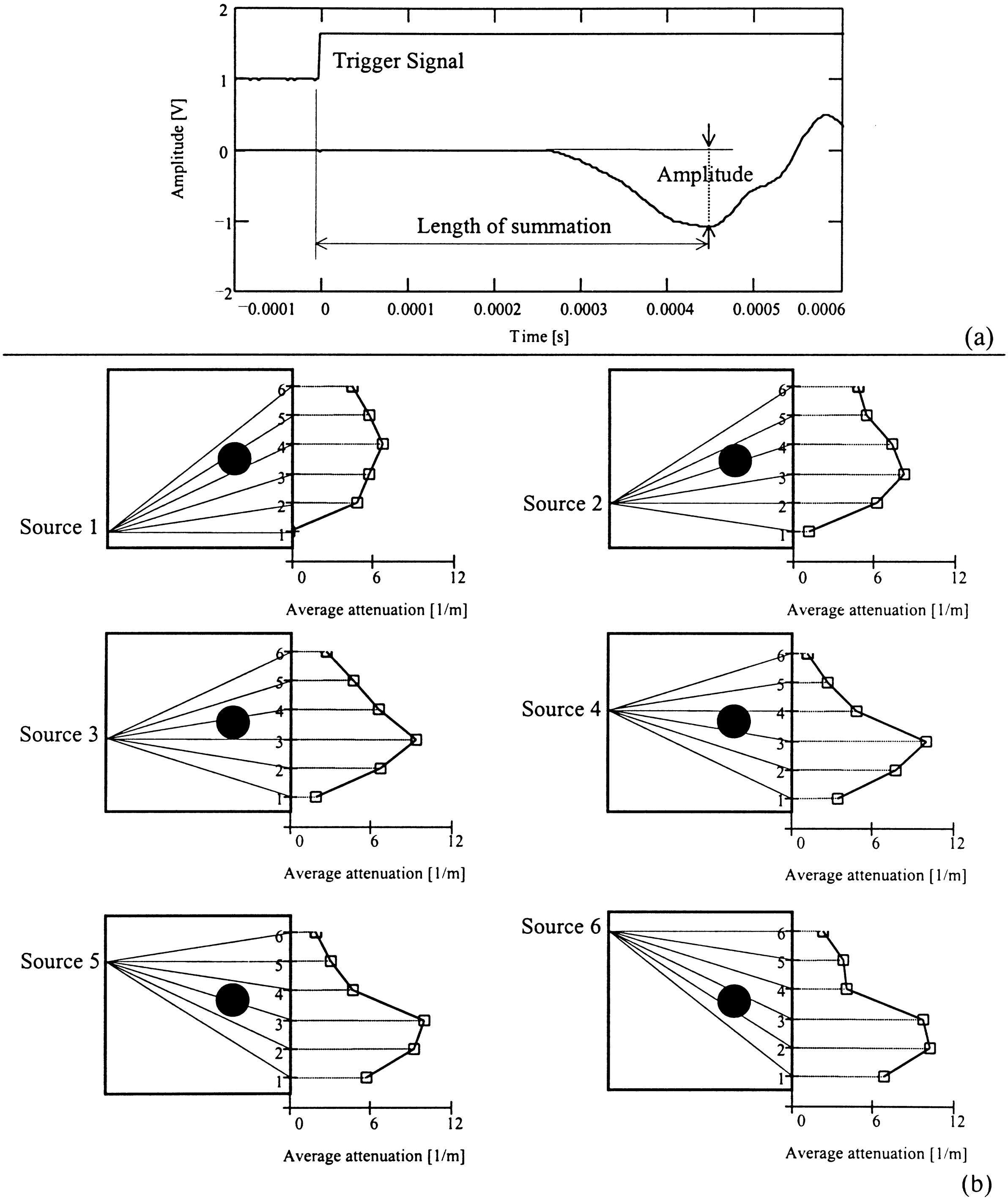

FIG. 5—*Amplitude data.* (a) *Determination of peak amplitude and energy. The amplitude method yields a more consistent data set.* (b) *Shadows of average attenuation for all sources; values are corrected for geometric spreading.*

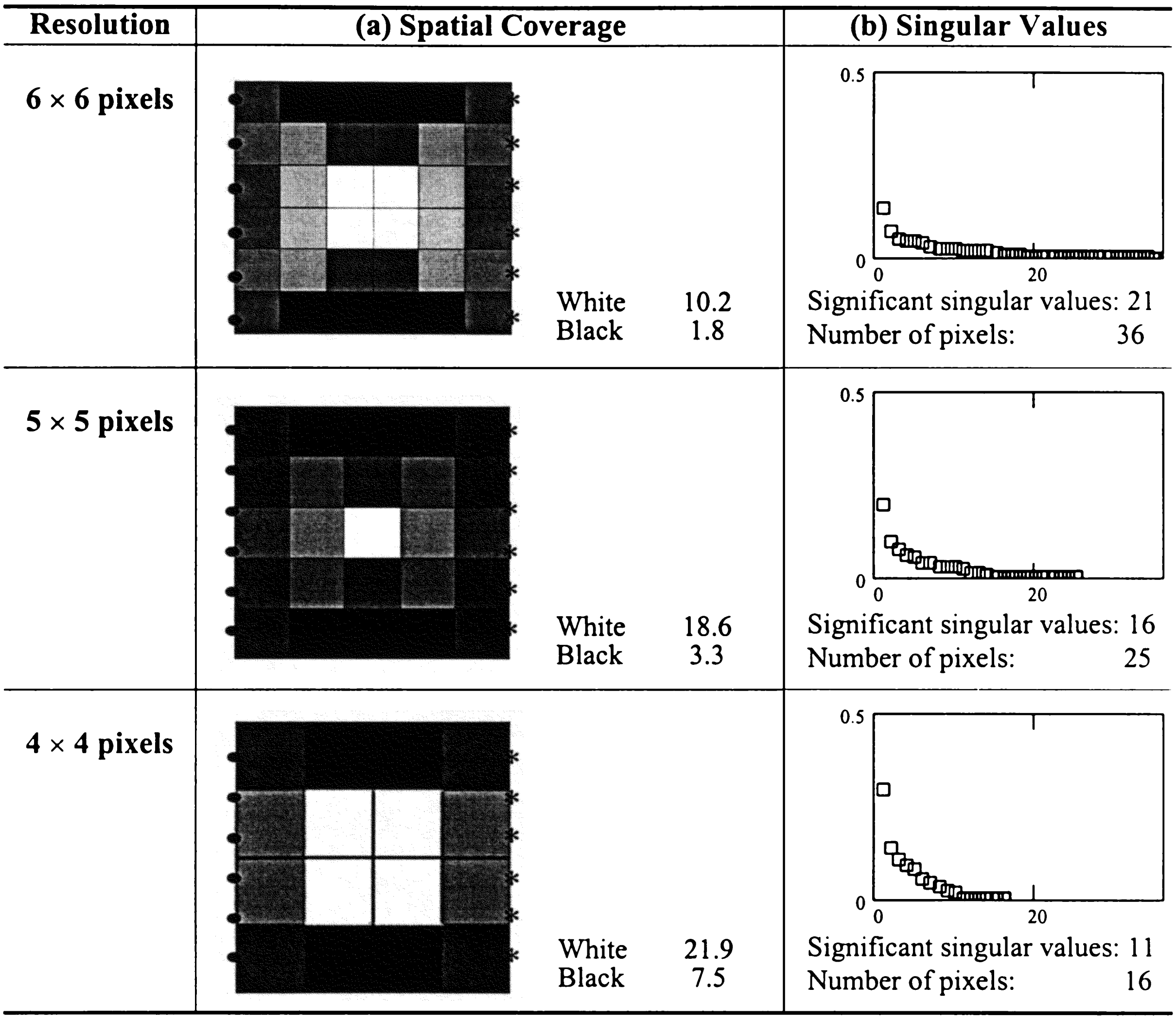

FIG. 6—*Data preprocessing.* (a) *Spatial coverage; the distance traveled in each pixel by all rays is normalized by the width of the pixel.* (b) *Singular values; as image resolution increases, the number of nonzero singular values increases but at a lower rate than the number of unknowns.*

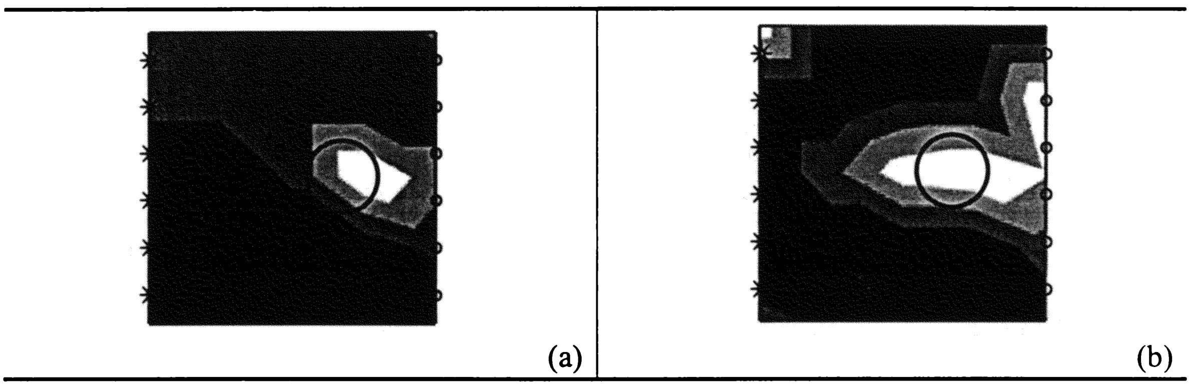

FIG. 7—*Initial guess from fuzzy logic constraining. 5×5 pixel resolution.* (a) *Velocity tomogram.* (b) *Attenuation coefficient tomogram.*

Fuzzy Logic—Figure 7 presents the analytically computed fuzzy logic images using both travel time and amplitude data for 5 × 5 pixel resolutions. The increase in resolution does not improve the image quality. In general, the solution obtained with amplitude data is of better quality than the solution obtained with travel time data. These results show the importance of contrast in the data between the background and the "shadow" caused by the inclusion. (Figs. 4 and 5).

Pixel-Based Tomographic Images

The regularized least squares solution with initial guess (Table 1) is used to compute the images shown in Figs. 8 and 9 (images obtained with other methods listed in Table 1 are of lesser quality). Fuzzy logic constraining (Fig. 7) provides the initial guess for the regularized least squares solutions. The regularization matrix is based on the smoothing operator. The regularization coef-

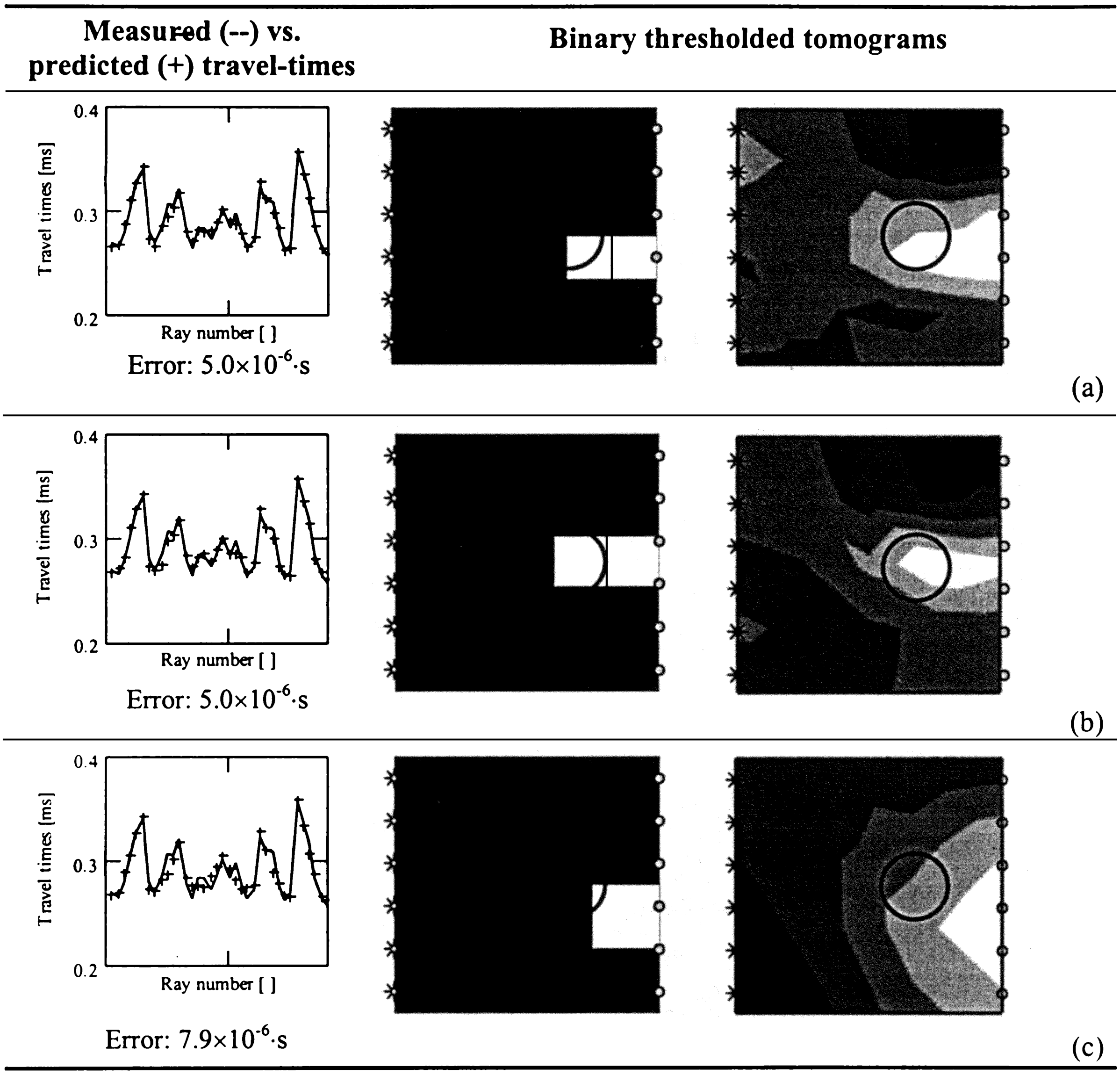

FIG. 8—*Velocity tomograms for different pixel resolutions. Regularized least squares solution with initial guess (regularization coefficient $\rho = 0.004$).* (a) *6×6 pixels.* (b) *5×5 pixels.* (c) *4×4 pixels.*

ficient controls the weight of the smoothing function into the final image. The selection of this coefficient is based in the quality of the image, the error in predicting the data, and the contrast between the largest and the smallest pixel value (for details see: Engl 1993; Gheshlaghi and Santamarina 1998; Santamarina and Fratta 1998). A high value of regularization renders an image with small contrast and a high residual while a small value of ρ results in a noisy image. In this study, a regularization coefficient $\rho = 0.004$ for travel time data and $\rho = 0.01$ for amplitude data yields the images that best fulfill the requirements of high contrast and small residual error.

Figures 8 and 9 present measured and predicted travel times, amplitudes, and the computed tomograms. The smaller number of pixels, the higher residual error—this is the tradeoff between the "degrees of freedom" in the solution (i.e., number of pixels) and the ability of the solution to match the data. Conversely, the higher the number of pixels, the less robust the solution becomes. Discretization of the space into pixels restricts the location of the inclusion.

Parametric-Based Inversion

Problems with the image quality and robustness in the inversion can be overcome by inversion based on the parametric representation of the medium. The same procedure applies to travel time or amplitude tomography, where velocities are substituted for attenuation coefficients. Five independent parameters define the properties of the medium and the inclusion (see Table 2 and Figs. 1*b* and 1*c*). Each parameter is successively perturbed. The L_2 error norm permits evaluating and guiding the convergence of the solution:

$$L_2 \text{ norm: } E = \frac{1}{N} \cdot \sqrt{\sum_{i=0}^{N-1} \left(t_i^{\langle\text{calc}\rangle} - t_i^{\langle\text{meas}\rangle}\right)^2} \qquad (12)$$

where $t_i^{\langle\text{meas}\rangle}$ is the measured parameter (travel time or amplitude), and $t_i^{\langle\text{calc}\rangle}$ is the calculated parameter. Convergence is improved if a proper initial guess is identified, for example, by fuzzy logic constraining (Fig. 7).

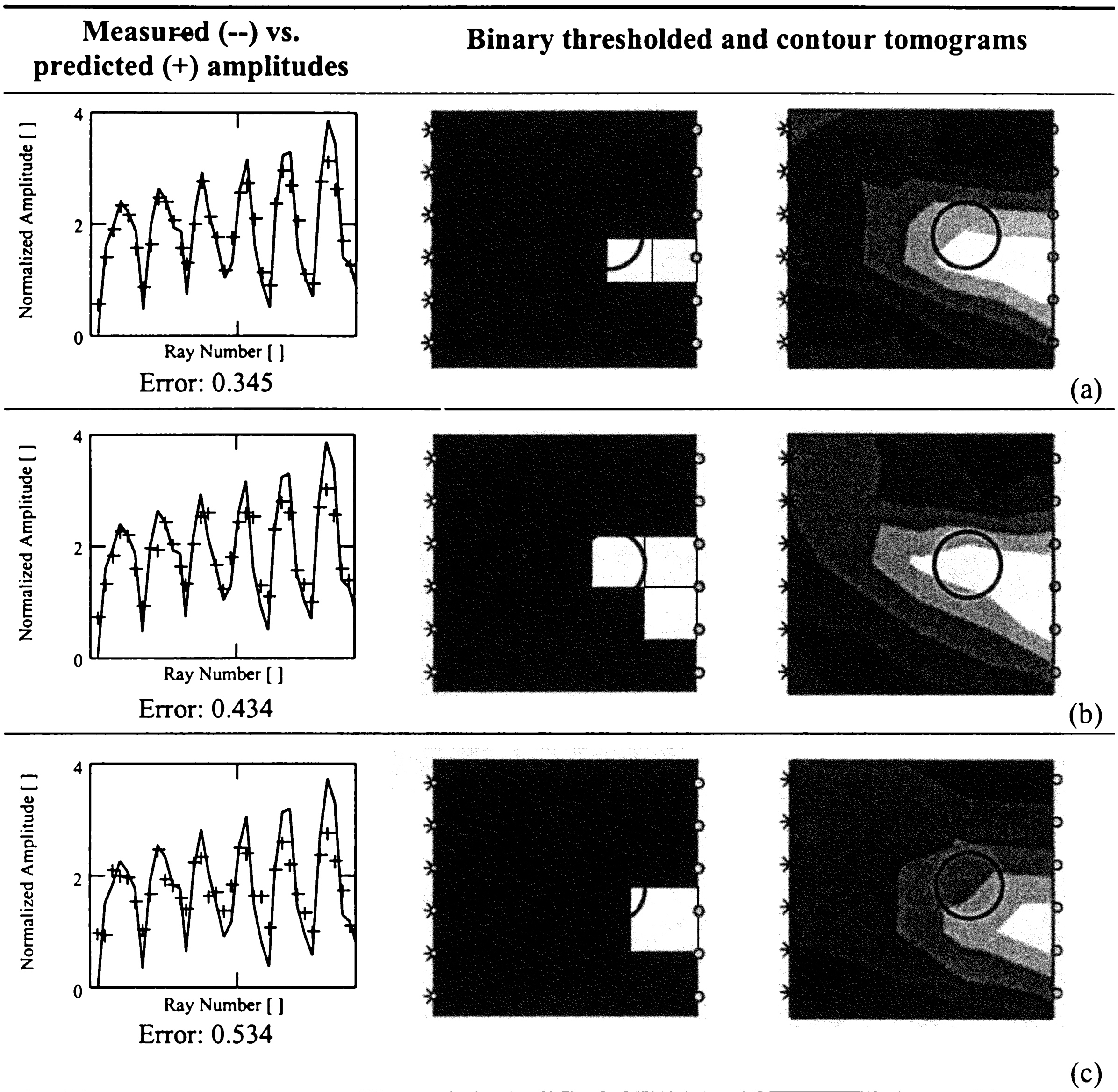

FIG. 9—*Attenuation coefficient tomograms for different pixel resolutions. Regularized least squares solution with initial guess (regularization coefficient* $\rho = 0.01$*).* (a) *6×6 pixels.* (b) *5×5 pixels.* (c) *4×4 pixels.*

Figures 10 and 11 present error functions near optimum for travel time and amplitude data using straight and curved rays. The straight-ray travel time solution shows excellent convergence for parameters V_{med}, y_{inc}, and R_{inc} (see Fig. 10). The convergence is weak for x_{inc}, as discussed in Santamarina and Reed (1994). Due to the use of straight rays, a velocity is computed for the inclusion (albeit with poor convergence) even though the void is not transversed by the wave front. The solution with curved rays avoids this physical pitfall. Furthermore, it permits inverting for edge velocity yet with very low convergence rate. In spite of this weak convergence, this result shows the importance of boundary conditions in the propagation of waves: as the wave propagates around the void, it samples the stress-free boundary, and the wave velocity decreases.

Figure 11 presents error functions near optimum for amplitude data using straight and curved rays. Trends and observations parallel those made in reference to Fig. 10.

Table 3 summarizes the geometric configuration of the medium inverted in all cases. Clearly, parametric inversion renders a very credible identification of the location and size of the anomaly, even though the data set is very small and it was gathered along restricted illumination directions. Other observations include: the poor resolution of x-position in the four cases, the tendency to underpredict the size of the low-velocity anomaly (diffraction healing), and the fairly limited advantages of curved rays even in this extreme case of an empty cavity. This last observation is based on the similarity in inverted parameters and residual error between curved and straight ray solutions.

Discussion: Proposed Methodology

The quality of the data is most important in any successful tomographic solution. This paper presents solutions using two types of data: travel time and amplitude. If the test methodology permits

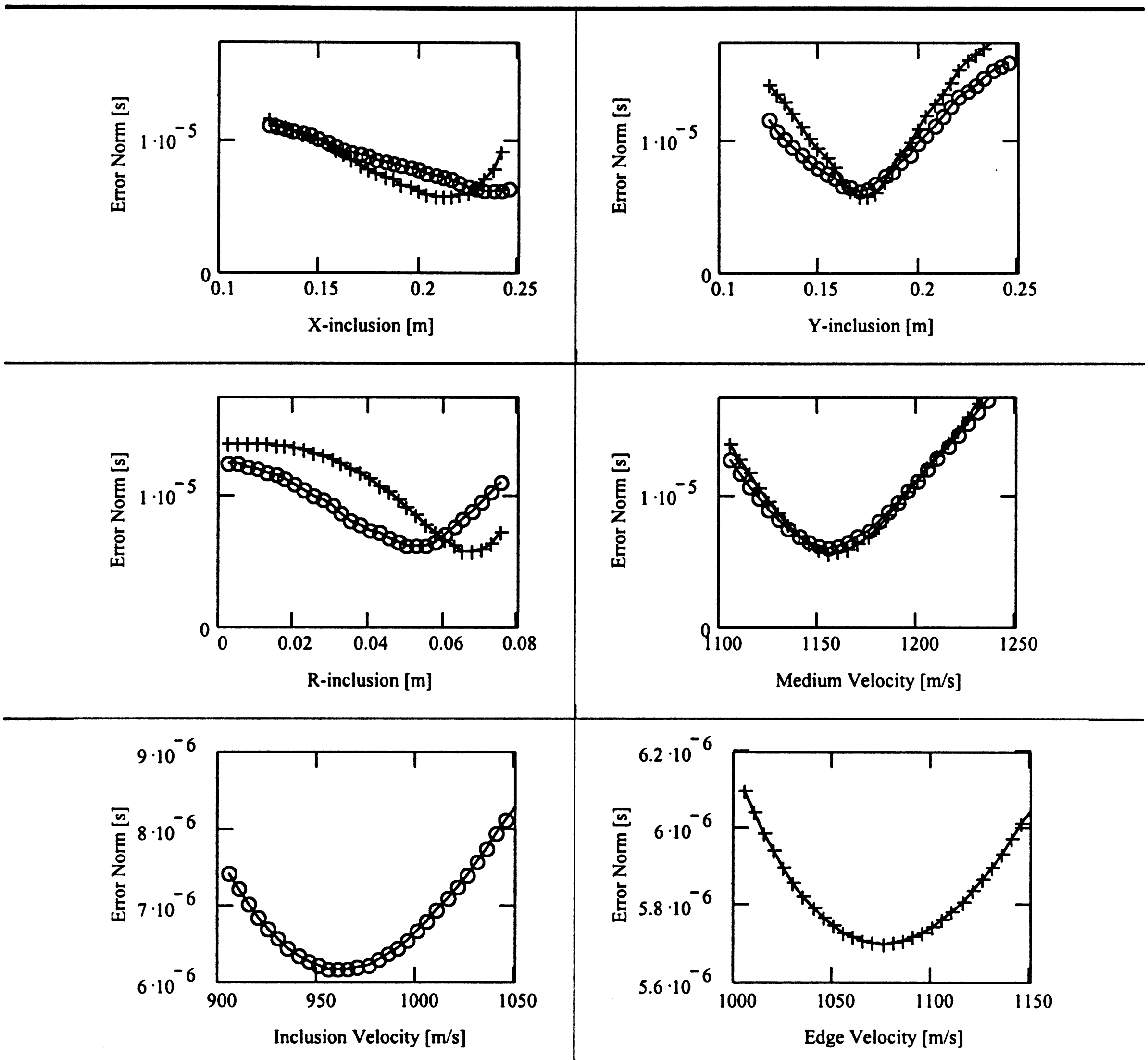

Inverted parameters using straight rays	**Inverted parameters using curved rays**
$V_{med} = 1150 \cdot m/s$ $V_{inc} = 960 \cdot m/s$	$V_{med} = 1160 \cdot m/s$ $V_{edge} = 1070 \cdot m/s$
$x_{inc} = 0.24 \cdot m$ $y_{inc} = 0.17 \cdot m$	$x_{inc} = 0.21 \cdot m$ $y_{inc} = 0.17 \cdot m$
$R_{inc} = 0.055 \cdot m$	$R_{inc} = 0.068 \cdot m$
Residual Error = $6.2 \times 10^{-6} \cdot s$	Residual Error = $5.7 \times 10^{-6} \cdot s$

FIG. 10—*Travel time data. Parametric inversion using straight rays (o–open circles) and curved rays (+-crosses). Note the scale for inclusion and edge velocities are different.*

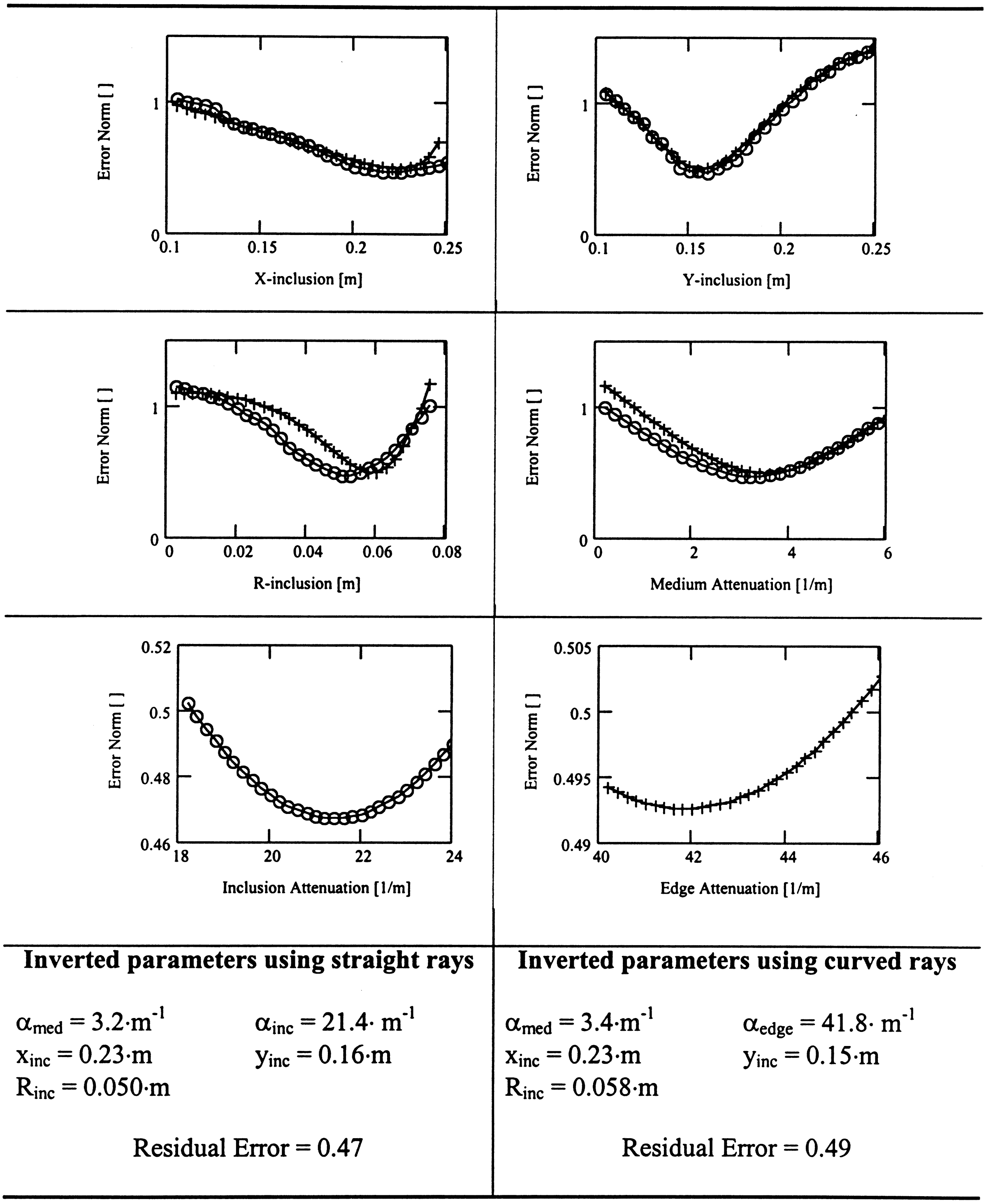

FIG. 11—*Amplitude data. Parametric inversion using straight rays (o–open circles) and curved rays (+-crosses). Note the change in scale for inclusion and edge attenuation.*

a consistent coupling between sources and receivers with the geotechnical structure (and the directivity of sources and receivers is known), amplitude data can provide high contrast projection or shadows.

While curved rays yield better results than straight rays because they match the physical reality closer, results presented in Figs. 10 to 11 and Table 3 show limited improvement in resolving the anomaly. Furthermore, the problem becomes nonlinear. Therefore, straight ray tomography can be "asymptotically" extended beyond its theoretical range, particularly in cases such as the one addressed here involving limited data sets and restricted illumination.

The solution based on the parametric representation of the medium is a very robust method of analysis. Figure 12 shows the variation of residual error with the number of unknown parameters for all cases considered in this study. The reduction of unknown pixel values decreases the resolution in the image and causes an increase in the residual error. However, adding information about the geometry of the problem, as done in parametric-based inversion, increases the robustness of the inversion while sharply decreasing the residual error. Still, the parametric solution is computer intensive due to the cost in forward simulations and the extent of the search space. The initial guess provided by fuzzy logic constraints permits reducing the cost of finding the solution.

TABLE 3—*Parametric inversion—Summary of inverted geometric parameters.*

Case	x_{inc}	y_{inc}	R_{inc}	Residual
Real conditions	0.19 m	0.18 m	0.076 m	n/a
Travel time				
straight	0.24 m	0.17 m	0.055 m	$6.2 \cdot 10^{-6}$ s
curved	0.21 m	0.17 m	0.068 m	$5.7 \cdot 10^{-6}$ s
Amplitude				
straight	0.23 m	0.16 m	0.050 m	0.47
curved	0.23 m	0.16 m	0.058 m	0.49

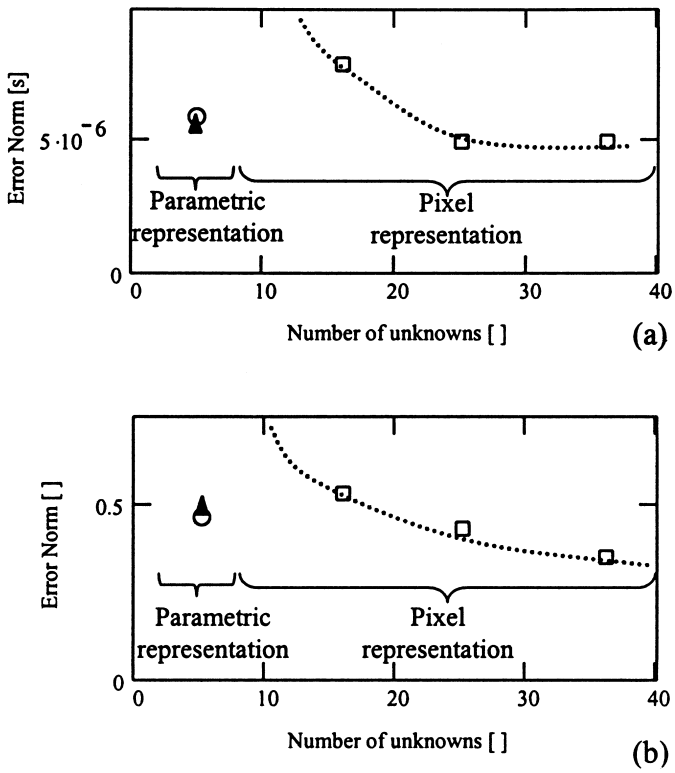

FIG. 12—*Residual versus number of unknown parameters.* (a) *Travel time data.* (b) *Amplitude data. The parametric inversion presumes a physical reality, thus, it leads to robust inversion even though the number of unknowns is small; furthermore, the residual is small (empty circle: straight rays; filled triangle: curved rays).*

Following this discussion, a methodology for tomographic imaging in civil/geotechnical structures with small data sets and restricted illumination can be extracted:

- Determine arrival times and amplitudes.
- Assuming straight ray propagation, use fuzzy logic constraining to obtain a credible initial guess.
- Use the fuzzy logic solution to determine an initial guess.
- Propose a simple model to represent the medium in terms of a small number of unknowns.
- Identify the optimal value of unknowns.
- If needed, convert this solution into a pixel representation, and use matrix inversion techniques to refine the solution.

Conclusions

An experimental study is conducted to identify the location of a low-velocity inclusion inside a concrete block. The anomaly is placed outside the region of maximum information. The modeled situation is similar to the presence of defects in piles, caissons, slurry walls, and other similar geotechnical systems. Elastic waves are used to "illuminate" the block. Both travel time and amplitude data are extracted.

The test configuration and alternative pixel resolutions are analyzed to assess spatial coverage and the number of singular values. Measurements are preprocessed with emphasis on the identification of shadows generated by the anomaly. The back-projection of these shadows helps constrain the presence of the anomaly, rendering a credible initial guess.

When the medium is represented in terms of pixels, the data are inverted with least-squares techniques implemented in matrix form. Regularization permits incorporating additional information into the problem, and it appears as the best inversion alternative for the mixed-determined cross-hole tomographic measurements.

When the medium is described in parametric form, the inversion of these parameters renders a very stable solution. The limited constraining of the anomaly in the direction of wave propagation is also manifested in this representation (i.e., limited x_{inc} resolution).

The combination of initial guess followed by inversion based on the parametric representation of the medium solution provides the most robust approach for the solution of the tomographic inversion of low-velocity inclusions in civil/geotechnical structures, with limited data sets and restricted illumination.

Acknowledgment

Support for this research was provided by the National Science Foundation and Georgia Institute of Technology. Reviewers made valuable comments and suggestions.

References

Devaney, A., 1984, "Geophysical Diffraction Tomography," *IEEE Transaction Geophysical Science. Special Issue in Remote Sensing*, Vol. GE-22, pp. 3–13.

Engl, H., 1993, "Regularization Methods for the Stable Solution of Inverse Problems," *Surveys in Mathematics for Industry*, Vol. 3, pp. 71–143.

Fratta, D., 1999, "Passive and Active Measurements of Unique Phenomena in Geotechnical Engineering." Ph.D. thesis, Georgia Institute of Technology, Atlanta, GA.

Gelius, L. J., 1995, "Limited-View Diffraction Tomography in a Non-Uniform Background," *Geophysics*, Vol. 60, No. 2, pp. 580–588.

Gheshlaghi, F. and Santamarina, J. C., 1998, "Data Pre-Processing in Cross-Hole Geo-Tomography," *Journal of Environmental and Engineering Geophysics*, Vol. 3, No. 1, pp. 41–47.

Kak, A. C. and Slaney, M., 1988, *Principles of Computerized Tomographic Imaging*, IEEE Press, New York, 329 p.

Llopis, J. L. and Ballard, R. F., 1995, "Crosshole Seismic Methods to Asses the Seismic Stability of Earthen Dams," *Proceedings of the Non-Destructive Evaluation of Aging Structures and Dams, SPIE Conference*, Oakland, CA, Vol. SPIE-2457, pp. 79–88.

Menke, W., 1989, *Geophysical Data Analysis: Discrete Inverse Theory*, Academic Press.

Nolet, G., 1987, "Seismic Wave Propagation and Seismic Tomography," *Seismic Tomography with Applications in Global Seismology and Exploration Geophysics*, G. Nolet, Ed., D. Reidel Publications Co.

Potts, B. D. and Santamarina, J. C., 1993, "Geotechnical Tomography: The Effects of Diffraction," *Geotechnical Testing Journal*, Vol. 16, No. 4, pp. 510–517.

Samani, A. M., 1997, "Travel-Time Tomography for Stress Reconstruction in Granular Soil Media," Ph.D. thesis, University of Waterloo, Waterloo, Ontario, Canada.

Samman, M. M. and O'Neil, M. W., 1997, "An Exercise in Seismic Testing of Drilled Shafts for Structural Defects," *Foundation Drilling*, December/January 1997, pp. 11–17.

Sansalone, M. and Carino, N. J., 1991, "Stress Wave Propagation Methods," *CRC Handbook on Nondestructive Testing of Concrete*, V. M. Malhorta and N. J. Carino, Eds., CRC Press, Boca Raton, FL, pp. 275–304.

Santamarina, J. C., 1994, "An Introduction to Geotomography," *Geophysical Characterization of Sites*, R. D. Woods, Ed., Oxford & IBH Publishing Co., New Delhi, pp. 35–44.

Santamarina, J. C. and Fratta, D., 1998, *Introduction to Discrete Signals and Inverse Problems in Civil Engineering*, ASCE Press, Reston, VA.

Santamarina, J. C. and Gheslaghi, F., 1995, "Tomographic Imaging: Potentials and Limitations," *Proceedings of the Non-Destructive Evaluation of Aging Structures and Dams, SPIE Conference*, Oakland, CA, Vol. SPIE-2457, pp. 297–302.

Santamarina, J. C. and Reed, A. C., 1994, "Ray Tomography: Errors and Error Functions," *Journal of Applied Geophysics*, Vol. 32, pp. 347–355.

Vasco, D. W., Peterson, J. E., and Mjer, E. L., 1995, "Beyond Ray Tomography: Wavepaths and Fresnel Volumes," *Geophysics*, Vol. 60, No. 6, pp. 1790–1804.

White, J. E., 1983, *Underground Sound. Application of Seismic Waves.* Elsevier, Amsterdam.

Wielandt, E., 1987, "On the Validity of the Ray Approximation for Interpreting Delay Times," *Seismic Tomography*, G. Nolet, Ed., Reidel Publishing Company, Dordrecht, pp. 85–98.

Wong, J., 1995, "Crosshole Seismic Tomography Across a Masonry Dam," *Proceedings of the Non-destructive Evaluation of Aging Structures and Dams, SPIE Conference*, Oakland, CA, Vol. SPIE-2457, pp. 58–66.